Optical Materials 155 (2024) 115832

Contents lists available at ScienceDirect

Optical Materials

journal homepage: www.elsevier.com/locate/optmat

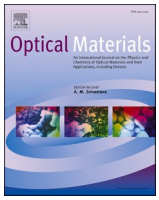

Research Article

"Enhancing wastewater treatment: DFT and experimental insights into ZnO-implanted TiO_2 Z-scheme photocatalyst mediated via *Smilax aspera*"

Mohamed Taha Yassin [a], Aayasha Negi [b,*], Sumit Ringwal [c], Minakshi Pandey [b], Prabhat Sati [d], Prashast Kumar Tripathi [e]

[a] *Botany and Microbiology Department, College of Science, King Saud University, Riyadh, 11451, Saudi Arabia*
[b] *Department of Chemistry IFTM University Moradabad, Uttar Pradesh, 244102, India*
[c] *Department of chemistry, Army cadet college, Indian Military Academy, Dehradun, 248007, India*
[d] *Department of chemistry S.G.R.R. PG college Dehradun, Uttarakhand, 248001, India*
[e] *H.N.B. Garhwal University, A central University Srinagar Garhwal, 246174, India*

ARTICLE INFO

Keywords:
Z scheme heterojunction
Photocatalyst
ZnO–TiO_2,DFT
Antifungal potential

ABSTRACT

This comprehensive study aimed to optimize the performance of photogenerated carriers in catalytic and optoelectronic systems by effectively separating electron-hole pairs. Green-synthesized TiO_2 nanoparticles (average size ~21 nm) and zinc acetate (99.5 % purity), augmented with eco-friendly integration of the plant *Smilax aspera*, resulted in a tailored hollow direct Z-scheme photocatalyst, ZnO–TiO_2, with adjustable ZnO loading ranging from 0.5 wt% to 5 wt%. Characterization techniques such as X-ray Diffraction, Fourier Transform Infrared Spectroscopy, Ultraviolet–Visible Spectroscopy, Transmission Electron Microscopy, Thermogravimetric Analysis and Energy-Dispersive X-ray Spectroscopy provided detailed insights into the atomic and electronic properties of the material. The analysis revealed the coexistence of anatase TiO_2 and wurtzite ZnO phases, each exhibiting distinct electronic band structures within the composite. Density functional theory calculated band gap values of 2.02 eV for TiO_2 and 2.89 eV for ZnO–TiO_2 corroborated the experimental results, offering a deeper understanding of electronic transitions within the heterojunction. The ZnO–TiO_2 composite showed significant photocatalytic efficacy in degrading Methylene Blue (98 % in 15 min) and Rose Bengal (79.69 % in 40 min) under UV light. It also exhibited antifungal potential against *Aspergillus niger* and *Candida albicans*, with inhibition zones of 28.0 ± 0.12 mm and 30.23 ± 0.68 mm, respectively. This research provides valuable insights into the eco-friendly, multifunctional applications of the ZnO–TiO_2 Z-scheme photocatalyst. This research thus provides valuable insights into the multifaceted applications of this synergistic, eco-friendly heterojunction photocatalyst in environmental remediation and its role as an effective antifungal agent.

1. Introduction

Ensuring access to clean water in the face of rapid global population growth and economic expansion is a pressing and complex challenge. The need to provide clean water is paramount, and addressing contaminants in freshwater sources and treating residual water has become crucial for maintaining the balance of the natural biosphere [1,2]. Traditional water treatment methods such as coagulation, flocculation, sedimentation, filtration, and disinfection have effectively removed many common water pollutants [3,4]. However, these methods have limitations when it comes to addressing persistent microscopic pollutants and emerging micro-contaminants like antibiotics, pesticides, and certain dyes. These substances are challenging to treat using traditional methods, necessitating exploration and implementation of advanced treatment technologies to effectively remove them from water sources. These pollutants are well-known for their harmful effects on the environment [5,6].

Extensive research has been dedicated to develop both conventional and cutting-edge treatment methods for the removal of persistent organic pollutants. Semiconductor heterogeneous photocatalysis, particularly Z-scheme heterojunction photocatalysts, has gained significant attention due to their superior oxidation and reduction rates compared to conventional type-II heterojunction materials. The Z-scheme heterojunctions establish a unique pathway for transporting

* Corresponding author.
E-mail address: aisha.negi04@gmail.com (A. Negi).

https://doi.org/10.1016/j.optmat.2024.115832
Received 29 March 2024; Received in revised form 12 July 2024; Accepted 15 July 2024
Available online 18 July 2024

photogenerated charge carriers, effectively enhancing redox capabilities and promoting efficient charge-carrier separation [7–9].

Titanium dioxide (TiO_2) is a widely recognized and dependable photocatalytic material for breaking down organic pollutants due to its non-toxic nature, high activity, excellent stability, and cost-effectiveness [10]. However, a drawback of single-phase $TiO_2$is the rapid recombination of photo-excited electron-hole pairs, hindering its photocatalytic activity. On the other hand, zinc oxide (ZnO) exhibits photocatalytic activity comparable to TiO_2 and is an attractive n-type semiconductor with advantages such as non-toxicity and high stability. This study presents a significant advancement where TiO_2 and ZnO together form a direct Z-scheme photocatalytic system. This innovative photocatalyst system leverages the enhanced reduction ability of photo-induced electrons in the ZnO conduction band (CB) and the heightened oxidation ability of photo-induced holes in the TiO_2 valence band (VB). Consequently, the photocatalytic properties of this Z-scheme system surpass those of conventional type-II heterojunction photocatalysts. This study successfully synthesizes ZnO–TiO_2direct Z-scheme heterojunction photocatalysts featuring a unique macro/mesoporous TiO_2 framework [11–14].

Utilizing Z scheme, which involves combine ZnO and TiO_2 instead of using ZnO individually, offers several advantages in photocatalysis. ZnO primarily absorbs light in the UV range due to its band gap of around 3.3 eV, while TiO_2 possesses a band gap of approximately 3.0 eV [15].When combined in a Z scheme, the effective band gap widens, enabling enhanced light absorption, particularly in the visible spectrum. This broader absorption range, resulting from the synergistic effects of their distinct bandgap energies in the Z scheme, leads to more efficient generation of electron-hole pairs and subsequent redox reactions, significantly improving the overall photocatalytic activity [16,17].

In the Z scheme, incident light excites electrons in both ZnO and TiO_2, generating electron-hole pairs. Electrons in the CB of one material can then transfer to the other, minimizing charge recombination and maximizing charge separation efficiency. These efficient charge dynamics, along with the widened effective band gap in the Z scheme, synergistically improve photocatalytic performance [18]. Additionally, the Z scheme configuration facilitates effective charge transfer and minimizes charge recombination, resulting in prolonged electron and hole lifetimes. These enhancements further elevate catalytic efficiency, making the Z scheme with ZnO and TiO_2 a highly effective solution for various photocatalytic applications.

In addition to this, fungal contaminants like *Candida albicans* and *Aspergillus niger* pose a significant threat in water treatment processes, necessitating thorough elimination. These fungi can contaminate water sources and pose health risks, especially for individuals with weakened immune systems or respiratory conditions. The contamination can occur through various pathways, including sewage, organic matter, and environmental exposure. Effective water treatment methods such as filtration, chlorination, ozonation, or UV disinfection are crucial for reducing or completely removing fungal presence, ensuring the safety of the water for consumption and minimizing health hazards [19,20].

ZnO and TiO_2 nanoparticles (NPs) are semiconductor materials with potent photocatalytic properties. When exposed to ultraviolet (UV) light, they produce reactive oxygen species (ROS) like hydroxyl radicals that have strong oxidizing abilities. These ROS can effectively break down the cell walls and membranes of fungi, rendering them inactive. Integrating ZnO and TiO_2 NPs into nanocrystals (NCs) or using them as coatings on filtration membranes enhances their ability to combat fungal contamination, allowing for efficient removal of fungal cells and spores during water treatment [21,22].

Recent studies have shown that combining TiO_2 with other semiconductors can significantly enhance its photocatalytic efficiency [23]. For instance, a report demonstrated that coupling TiO_2 with ZnO in a Z-scheme configuration improved the degradation of organic pollutants under UV light due to enhanced charge separation and prolonged electron-hole lifetimes [24].Similarly, another reported work has shown a TiO_2-ZnO heterojunction exhibited better photocatalytic activity than pure TiO_2 or ZnO, attributing this to the synergistic effect of the two materials, which enhanced light absorption and reduced recombination rates [7].This innovative photocatalytic approach offers a promising and sustainable solution to address fungal contamination in water.

The synthesis process adopts environmentally friendly methods, ensuring the eco-friendliness of the photocatalysts. Amidst efforts towards effluent recycling, a new challenge has emerged: mitigating the harmful effects of microorganism infection. The “Green Method,” utilizing plant resources to create NPs, offers a promising solution to this ongoing issue. Green methods, being economical, chemical-free, and environmentally benign, prioritize generating the necessary output without employing hazardous intermediates [25–27].In this study roots of *Smilax aspera* were employed for the synthesis of NCs. *Smilax aspera*, commonly known as “Rough Bindweed” or “Rough *Smilax*,” is a medicinal plant with a rich pharmacological profile. Its potential medicinal properties are attributed to a diverse array of phytoconstituents, including saponins, flavonoids (quercetin, kaempferol), alkaloids (smilagenin, sarsaparilloside), tannins, phenolic compounds, terpenoids, and essential oils. These bioactive compounds contribute to the plant’s therapeutic effects, encompassing anti-inflammatory, antioxidant, antimicrobial, anticancer, hepatoprotective, diuretic, analgesic, antipyretic, immunomodulatory, and antidiabetic activities. *Smilax aspera* thus stands as an intriguing subject for further research and exploration, promising potential benefits for various health applications. This integrated approach emphasizes both advanced technology and sustainable, environmentally friendly practices for effective water treatment and environmental preservation [28–30].

2. Experimental section

2.1. Material collection

- **Plant:**Roots of *Smilax aspera* were gathered from Bairgaun (1499 m) pauri Garhwal Uttarakhand.
- **Reagent:**

Zinc acetate (Zn $(CH_3COO)_2.6H_2O$) Sigma Aldrich, TiO_2 (Merck), NaOH, Methylene blue (MB) ($C_{16}H_{18}ClN_3S$), ($C_{20}H_2Cl_4I_4Na_2O_5$) Rose Bengal (RB) were acquired from Fischer Scientific. The experiment employed double-distilled water throughout.

- **Fungal pathogen:**

Candida albicans ATCC-10231 and *Aspergillus niger* ATCC-16404 were sourced from CSIR-NCL, Pune, Maharashtra, India.

2.1.1. Plant extract preparation

The freshly harvested roots were meticulously cleansed using distilled water to remove any adhering impurities. Subsequently, the roots were subjected to an air-drying process to ensure complete desiccation and removal of residual moisture. The desiccated roots were finely powdered using a mechanical grinder, yielding a finely particulate powder that served as the foundation for all ensuing scientific inquiries. To formulate the method [31] was employed after slight modifications varying concentrations of the root extract solution (3 %, 5 %, 7 %, and 10 % w/v), precisely 250 mL of distilled water was introduced into a 500 mL Erlenmeyer flask. The solution was then subjected to controlled heating at 60 °C, maintaining this temperature for a duration of 30 min. After post-heating, the extract was allowed to achieve thermal equilibrium with the surroundings before being meticulously filtered using Whatman no.1 filter paper, ensuring a refined solution. The resultant concentrate was meticulously stored at a temperature of 4 °C to preserve its integrity for subsequent rigorous scientific analysis and experimentation.

2.1.2. Synthesis ZnO–TiO_2

The obtained filtrate was employed in the synthesis of ZnO–TiO_2, as elaborated in Fig. 1. For the solution preparation, 20 mL of SA roots extracts, 70 mL of distilled water, and 3 g of $Zn(CH3COO)_2•2H_2O$ were combined. The solution was stirred consistently at a fixed temperature of 90 °C. Following 30 min of heating, TiO_2 was introduced into the ZnO solution. To create the TiO_2 solution, 3 g of TiO_2 powder was mixed with 10 mL of distilled water and homogenized for 5 min using a magnetic stirrer set at a constant speed of 200 rpm. NaOH was then gradually added drop by drop until the pH reached 7. The resulting mixture was continuously heated and stirred overnight, resulting in the formation of a paste. The sample paste was subsequently dried in an oven for 8 h to obtain ZnO–TiO_2 powder. The powder was then subjected to centrifugation at 5000 rpm for 20 min, following the procedure illustrated in Fig. 1.

2.2. Sample characterization

The biosynthesis process of ZnO–TiO_2 NCs was meticulously monitored using advanced characterization techniques. High-resolution UV–Visible spectrometry was performed using an Elico SL spectroscope, covering the wavelength range of 200–800 nm. Fourier transform infrared spectroscopy (FTIR) with PerkinElmer ES Spectrum 2.0 software was utilized to analyze the surface adsorption of functional groups on the biosynthesized NPs, covering the range of 450–4000 cm^{-1} with a resolution of 4 cm^{-1}.

For structural analysis, a PANalytical X'PERT PRO X-ray diffractometer with CuK radiation of 1.54 Å wavelength was employed to examine the purified powders. Additionally, X-ray diffraction data (XRD) of the NCs were obtained using a Philips PRO expert diffractometer, utilizing nickel-filtered CuK radiation, operated at a voltage of 40 kV and a current of 30 mA. These methodologies facilitated a comprehensive exploration of the structural attributes of the bio-synthesized ZnO–TiO_2 NPs.

Scanning electron microscopy (SEM) with energy-dispersive X-ray (EDX) analysis involved examining samples using a SEM Quanta 200 with an EDX system. The NPs colloid was deposited onto a carbon grid and dried under low vacuum conditions (10–130 pa), maintaining a voltage of 20 KeV. The initial sample scanning was conducted at a magnification of 3000×, followed by focused analysis using the EDX system to confirm the presence of elements. Furthermore, the NP samples were placed on a carbon-coated copper grid and scanned using the FEI Tecnai TF20 equipped with a 200 kV FEG source, a ± 70° tilted computer-controlled stage, and a 4K × 4K Eagle CCD Camera with a 4-port readout and a 15 μm pixel size. EPU software was employed for in-depth data exploration. Transmission Electron Microscopy (TEM) images were scanned over JEOL JEM-1400 TEM, at an accelerating voltage of 120 kV.

To assess thermal stability, Thermogravimetric Analysis (TGA) was performed using the TGA 2950 Thermogravimetric Analyzer. These intricate characterization techniques collectively enabled an exhaustive examination of the NCs morphology, composition, and thermal behaviors.

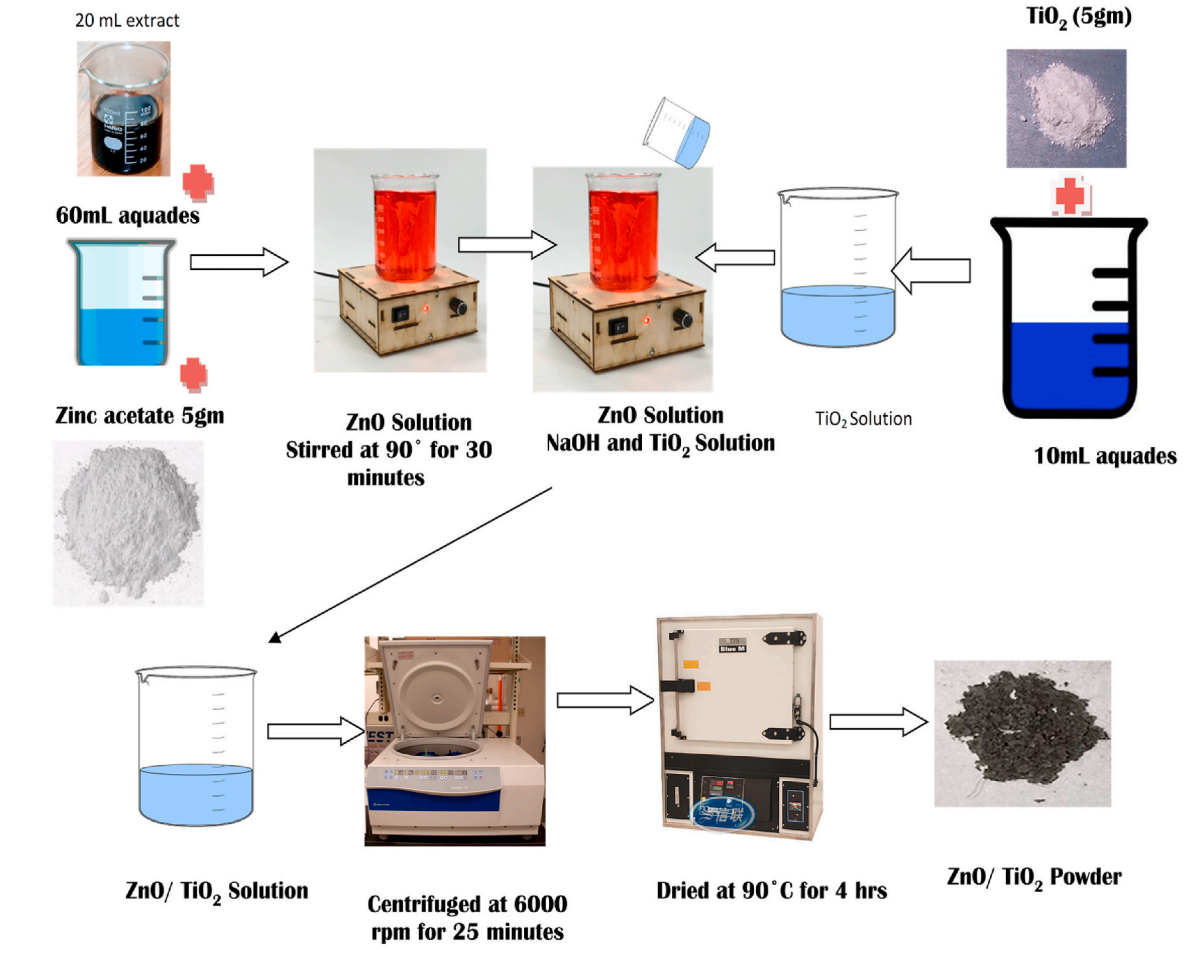

Fig. 1. Schematic presentation of formation of ZnO–TiO_2.

2.3. Computational study

Our investigation began with careful preparation of accurate crystal structure details for the ZnO–TiO_2. Quantum ESPRESSO software and density functional theory (DFT) calculations were used to explore the energy landscape. The PBE (Perdew-Burke-Ernzerhof) exchange-correlation functional, incorporating van der Waals interactions, was applied [32,33]. Geometry optimization at 300K and 700K using the BFGS algorithm revealed stable atomic configurations. Thermodynamic properties such as Gibbs free energies were computed, shedding light on essential characteristics. Equilibrium calculations led to the formation of a triangular phase diagram, illustrating stability regions and coexistence spaces.

Simultaneously, the study delved into the combination of ZnO and TiO_2, analyzing electronic band structures and their alignment. Crystal models for both were constructed using VESTA based on XRD data parameters. The simulation utilized the GGA-PBE exchange-correlation functional, norm-conserving pseudopotentials, and accounted for electron spin polarization. Geometry optimization employed the BFGS method with a plane wave expansion energy cutoff of 750 eV. Monkhorst-Pack (MP) k-point spacings of 0.125/Å and 0.0125/Å were employed for geometry optimization, band structure, and density of states (DOS) calculations. The choice of method was guided by its suitability for semiconductor systems and the balance between accuracy and efficiency. These comprehensive studies contributed to an enhanced understanding of $ZnTiO_3$ and the combined ZnO–TiO_2 system through advanced calculations and insightful analysis.

2.4. Dye degradation

Photocatalytic degradation of RB and MB dyes using ZnO, TiO_2NPs, and a ZnO–TiO_2 composite were investigated under solar light exposure using earlier employed method [34,35].ZnO (0.5 g), TiO_2 (0.5 g), and ZnO–TiO_2 (1.0 g) were dispersed in 100 mL of deionized water via ultrasonication for 30 min. Stock solutions of RB and MB dyes (10 ppm) were prepared. 50 mL of the dye solutions were mixed with their respective NPs in 100 mL glass beakers. The pH of each solution was adjusted to 7 using buffer solutions to ensure optimal reaction conditions. The mixtures were exposed to solar light for 4 h. Samples (5 mL) were collected every 30 min and centrifuged at 3000 rpm for 10 min to separate NPs and any solid residues from the supernatant. Dye concentrations in the supernatant were determined using a UV–Visible spectrophotometer at 664 nm for MB and 543 nm for RB [36–38]. In conclusion, this study systematically examined the efficiency of ZnO, TiO_2, and ZnO–TiO_2 composites in the photocatalytic degradation of RB and MB dyes. The results, as reflected in the degradation kinetics, offer valuable insights into the potential applications of semiconductor NPs in environmentally friendly wastewater treatment processes.

2.5. Antifungal activity

To assess the antifungal potential of ZnO, TiO_2, and their composite ZnO–TiO_2 we employed the previous reported method [28].We utilized a modified well diffusion method to evaluate the antifungal activity. The fungal pathogens were cultured in Sabouraud's dextrose agar/broth, and after 48–72 h of incubation, the cultures were transferred to Sabouraud's dextrose agar medium for an additional 48 h at 28 °C to allow for fungal growth. To test the antifungal properties, we prepared test samples of NPs at a concentration of 1 mg/mL, dissolved in dimethyl sulfoxide (DMSO). Wells of specific diameter were carefully punched into the agar, and each well was loaded with the respective nanoparticle sample. For comparison, we included a well with Fluconazole (1 mg/mL), a recognized antifungal agent. Additionally, a well filled with DMSO served as the negative control [39].After incubation at 28 °C, the clear zones of inhibition around the wells were measured. The diameter of the inhibition zones was indicative of the antifungal activity. A zone equal to or larger than that of Fluconazole was considered as potent antifungal activity for the respective NPs. This method provided insights into the potential of these NPs as antifungal agents and their efficacy compared to a standard antifungal drug.

3. Result and discussion

3.1. Characterization results

3.1.1. UV–visible spectroscopy and XRD study

The ZnO–TiO_2heterojunction composite prepared in this study exhibited a slight red-shift in comparison to the absorption peaks of pure TiO_2 and ZnO NPs as can be seen in Fig. 2. The absorption peaks in the UV range were attributed to the TiO_2 phase, while the peak in the visible region was attributed to ZnO. Through experimental determination, the optical band gaps (Eg) for all the three types of samples were estimated. The pure TiO_2NPs had an Eg value of 2.3 eV, while the ZnO-NPs had an Eg value of 2.2 eV. These values are consistent with previous reports [40].The slight difference in the Eg values further supports the successful formation of the ZnO–TiO_2heterojunction composite [17,18].

As shown in Fig. 3(a) XRD analysis indicates a significant overlap between the (102) and (103) crystal planes of ZnO and the (200) and (204) planes of TiO_2. This pronounced overlap strongly suggests a robust interaction within their respective lattice structures, affirming the successful formation of the ZnO–TiO_2 composite. Additionally, minor peaks observed at $2\theta(^o)$ angles of 30.14, 42.96, 50.78, and 60.70 correspond to the crystal planes (220), (400), (422), and (440), respectively, corroborating the presence of the $ZnTiO_3$ phase (JCPDS card No: 39–0190). The lattice spacing values of 0.35 nm and 0.26 nm observed in the XRD patterns of pure TiO_2 and ZnO, respectively, closely align with those reported for TiO_2 (JCPDS 21–1272) and ZnO (JCPDS 89–1397) [41]. Importantly, the absence of any impurity phase confirms the two-phase composition of the synthesized heterojunction composite. These XRD findings furnish compelling evidence for the successful fabrication of the ZnO–TiO_2 composite, highlighting distinct lattice interactions and the presence of two well-defined phases.

ZnO–TiO_2 has an ilmenite structure, trigonal $\overline{R}$ 3 space group. Ti^{4+} bonds to six O^{2-} forming TiO_6 octahedra, sharing corners with nine ZnO_6 octahedra. Tilt angles range from 45 to 61°. Zn^{2+} bonds to six O^{2-} forming ZnO_6 octahedra. Bond lengths: Ti–O (1.89 Å, 2.11 Å), Zn–O (2.05 Å, 2.26 Å). O^{2-} forms a mix of edge and corner-sharing OTi_2Zn_2 trigonal pyramids as shown in Fig. 4.

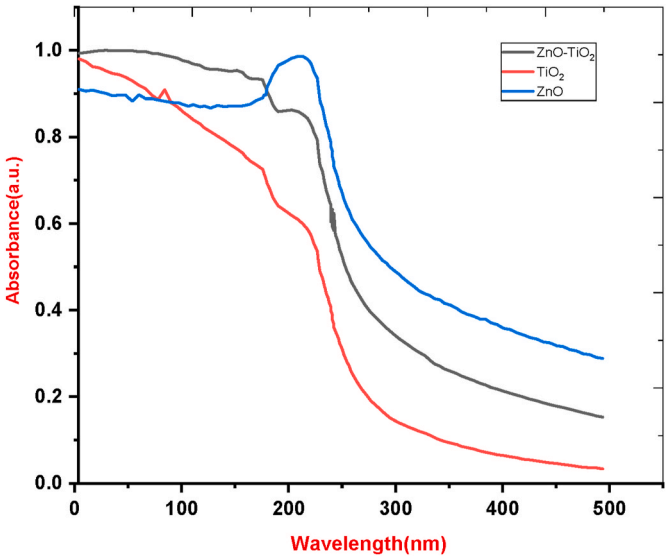

Fig. 2. UV–Vis spectra of ZnO,TiO_2&ZnO–TiO_2.

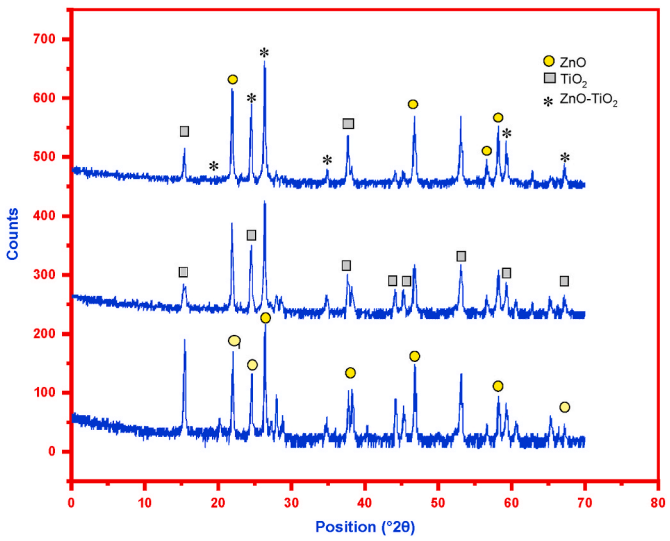

Fig. 3. (a). XRD spectra of ZnO, TiO_2&ZnO/TiO_2.

3.1.2. FTIR spectroscopy and TGA analysis

The FT-IR analysis encompassed both pure TiO_2 and pure ZnO samples, depicted in Fig. 5(a). In the FTIR spectrum for ZnO, discernible peaks correspond to specific vibrational bands related to diverse functional groups. Notably, the peak at approximately 3442.20 cm^{-1} is likely attributed to O–H stretching, indicative of hydroxyl groups or water presence. Similarly, at 1684.22 cm^{-1}, the peak implies C═O stretching, possibly originating from carbonyl groups such as aldehydes or ketones [42].Moreover, the peak at 1432.05 cm^{-1}suggests C–H bending, potentially indicating the presence of methyl or methylene groups. Additionally, the peak at 1087.32 cm^{-1}corresponds to C–O stretching, suggesting the presence of alcohol, ether, or ester groups, while the peaks at 725.03 $cm^{-1}$and 559.05 $cm^{-1}$are likely associated with O–H bending vibrations [43,44].In the FTIR spectrum of the ZnO–TiO_2 composite, distinctive vibrational wavenumbers were identified, each indicative of specific functional groups or molecular interactions. The wavenumber at 553.864 cm cm^{-1}signifies metal-oxygen (M – O) stretching, characteristic of the composite's structure [45]. [][][]At 88.016 cm^{-1}, the composite exhibits potential lattice vibrations or other structural features. Moreover, the vibrational wavenumber at 1095.74 cm^{-1} suggests C–O stretching, potentially originating from carbonates or organic compounds [46].Additionally, the peak at 1434.54 cm^{-1}implies C–H bending vibrations, often found in hydrocarbons or alkanes. The wavenumber 1665.38 cm^{-1} is consistent with C═O stretching, suggesting the presence of carbonyl groups, potentially from aldehydes or ketones. Furthermore, the peak at 2949.53 cm^{-1}implies C–H stretching vibrations, common in hydrocarbons or alkanes [47]. Lastly, the wavenumber 3411.35 cm^{-1}indicates O–H stretching, pointing to the presence of hydroxyl groups or water in the composite. These identified wavenumbers and associated functional groups provide essential insights into the molecular composition and structure of the ZnO–TiO_2composite, contributing to a deeper understanding of its properties and potential applications. Further analysis and comparison with known vibrational frequencies for specific functional groups would enhance the interpretation. The analysis of individual TiO_2-FTIR spectrum revealed peaks corresponding to specific functional groups. For instance, the peak at approximately 3171.68 cm^{-1} indicates N–H stretching, suggesting the presence of amines or amides. Similarly, around 1587.67 cm^{-1}, the peak is indicative of C═C stretching, often found in aromatic rings. At 1477.51 cm^{-1}, C–H bending vibrations in aromatic compounds are suggested. The peak at 1092.11 cm^{-1} corresponds to C–O stretching, pointing towards alcohols, ethers, or esters [48,49].Lastly, at 770.51 cm^{-1}, Ti–O stretching vibrations are indicated. These assignments provide valuable insights into the molecular composition and potential bioactive compounds present in the samples, supporting the absorption of bioactive compounds on the surface [50] as depicted in Fig. 5(a).& Fig. 5(b). Thermal stability of synthesized nanomaterial was estimated with the help of TGA, obtained results shows stability of ZnO NPs till 300 °C but sharp change of 25 % mass loss was reported till 400 °C which again fall rapidly, and it was observed that mass loss reach 29 % when temperature was 800 °C,TiO_2 17 % of mass loss was observed till 400 °C which fall gradually and mass loss was reported 34 % when temperature reach 800 °C·ZnO–TiO_2 there was no significance mass change till 300 but mass loss of 18 % was estimated at

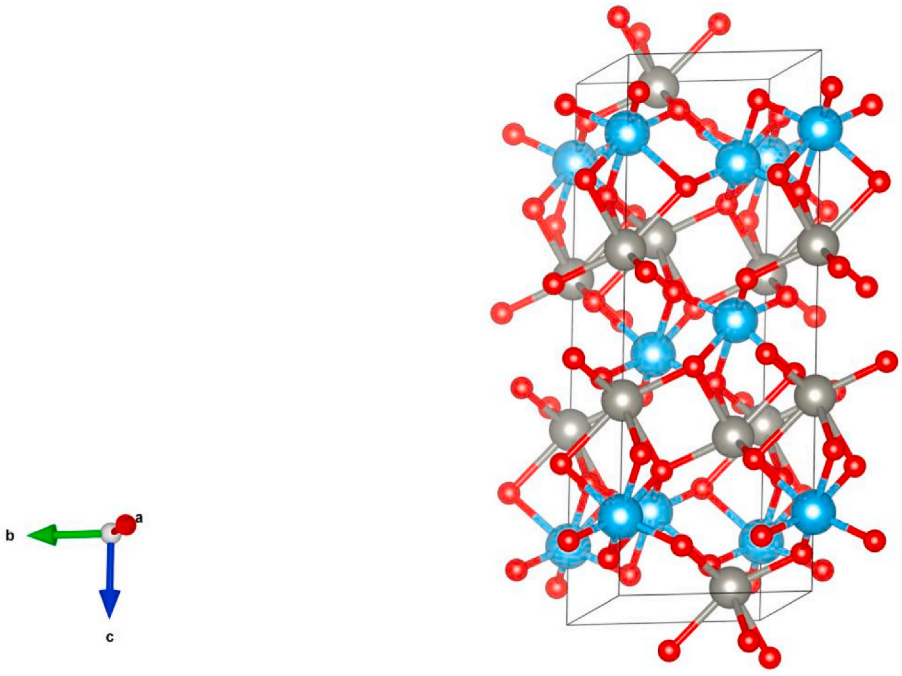

Fig. 4. Crystal structure of ZnO–TiO_2.

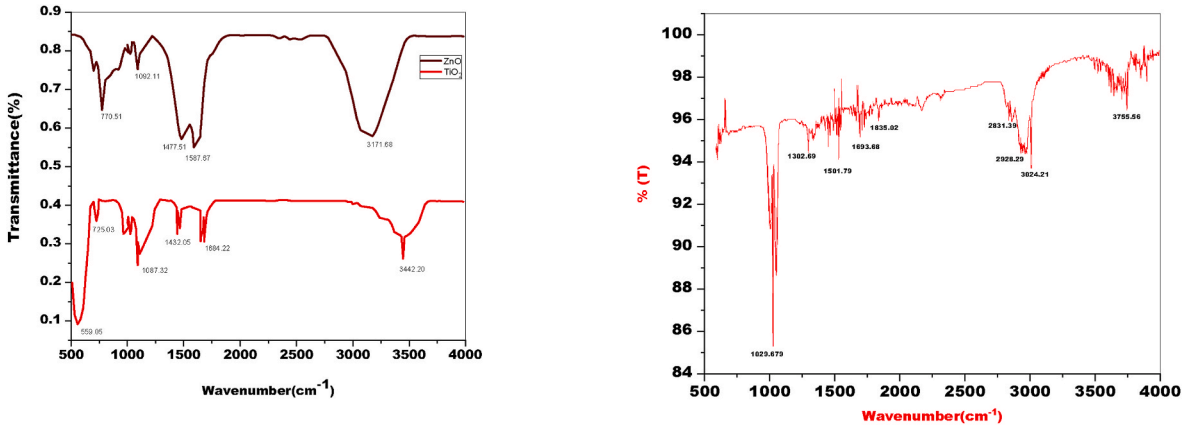

Fig. 5. (a). FT-IR spectra of ZnO&TiO_2 Fig. 5.(b). FT-IR spectrum of ZnO–TiO_2.

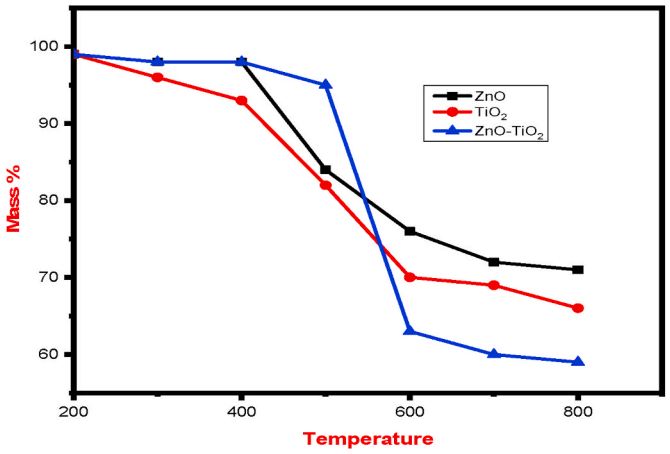

Fig. 6. TGA of ZnO, TiO_2 & ZnO–TiO_2.

400°Ceven after that sharp mass change was found and it reach 41 % when temperature was 800 °C (see Fig. 6).

3.1.3. EDX and TEM studies

The EDX analysis Fig. 7 Confirms the presence of Ti, Zn, and O elements, indicating a uniform distribution of these elements within the heterojunction composite. This uniformity ensures consistent performance across the material.

TEM images Fig. 8 shows a regular microporous structure in the TiO_2 matrix, further validating the high surface area and effective morphology of the NC. The combination of EDX and TEM results corroborates the successful synthesis of the ZnO–TiO_2 NC, demonstrating the integration of ZnO into the TiO_2 matrix and highlighting the material's potential for various applications.

3.2. Computational study

3.2.1. Compositional phase diagram

The triangular phase diagram Fig. 9 Obtained through DFT analysis provides valuable insights into the thermodynamic stability and potential phase transitions of a compound at different temperatures [51]. The complexity of the phase diagram at 300K, with 15 phacets, suggests that the compound demonstrates intricate behavior at this temperature. Each phacet represents a distinct stable or metastable phase that can coexist within the given conditions. Conversely, the phase diagram at 600 K, characterized by 12 phacets, indicates a reduction in the number of stable and metastable phases as temperature increases. This observation implies that certain phases or configurations that were stable at 300K become less prevalent or unstable at 600K. This transition could result from changes in molecular interactions, crystal structures, or chemical bonding due to the heightened thermal energy. This phenomenon indicates that certain compounds or phases may become thermodynamically unstable under the conditions of 600K, leading to their decomposition into other forms or their transformation into more stable phases. The decrease in the number of stable phases highlights the influence of temperature on the equilibrium between different chemical species and their respective phases.

In summary, this triangular phase diagram offers a comprehensive view of the compound's response to temperature variations. The diminishing number of phacets as temperature rises underscores the evolving nature of its stability landscape [52].

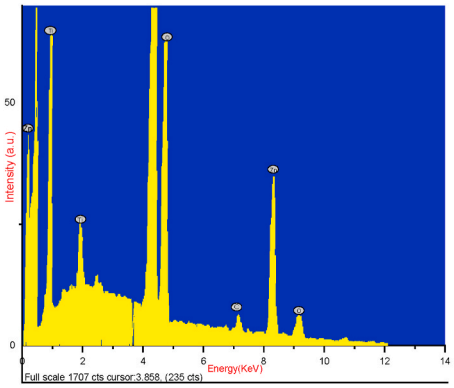

Element	At (%)
O	38.62
Ti	29.35
Zn	27.03
C	5`

Fig. 7. EDX analysis of ZnO/TiO_2.

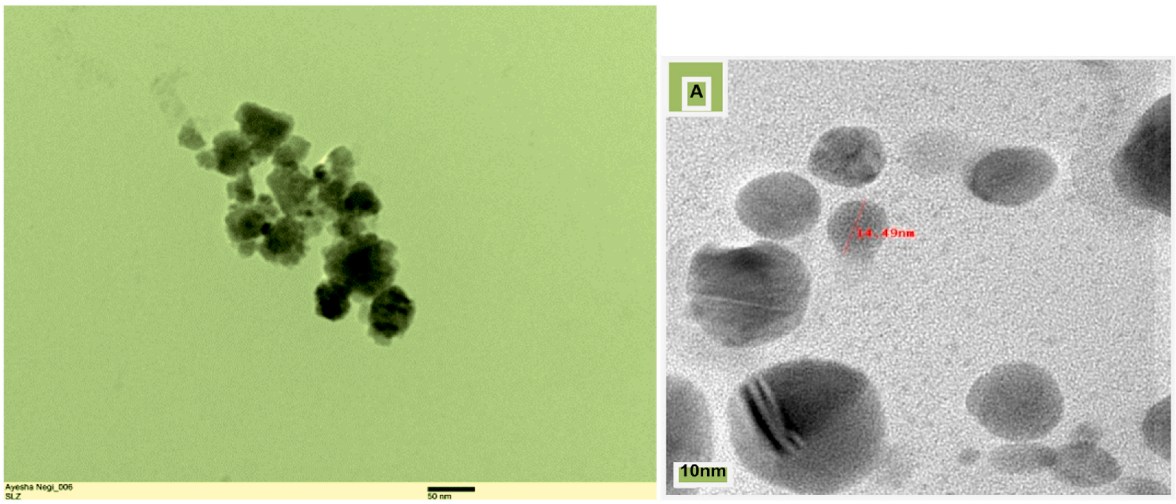

Fig. 8. TEM images of ZnO–TiO_2at 15000x and 30000× magnification respectively.

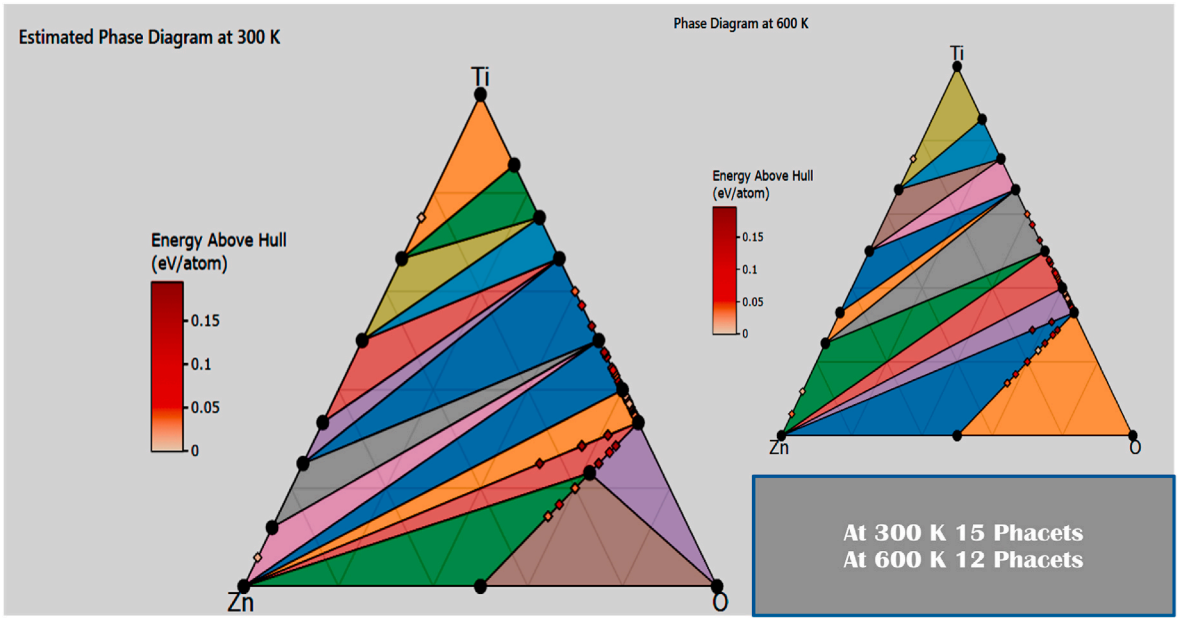

Fig. 9. Phase diagram at 300K and 600K

3.2.2. *Band gap and density of state*

Fig. 10 illustrate the band structures of TiO_2 and ZnO–TiO_2, respectively. In TiO_2, the Fermi level resides at the valence band maximum (VBM), whereas in ZnO–TiO_2, electronic states are denser in both the conduction band minimum (CBM) and VBM, leading to new states near the VBM. These states emerge from impurity levels. Notably, the CBM edge of ZnO–TiO_2 has shifted compared to the Fermi level, indicating the activity of electrons (e^-) and holes (h^+) near the CBM and VBM. The calculated energy gap of TiO_2 was 2.02eV while experimental UV–Vis results for TiO_2 showed 2.3 eV, with theoretical values often lower than experimental ones. In line with the ZnO–TiO_2 structural model the calculated band gap for ZnO–TiO_2 was 2.89 eV. These calculated results align well with established experimental data.

3.3. *Dye degradation*

The photocatalytic performance of ZnO–TiO_2 materials in degrading dyes was assessed using a UV–Vis spectrophotometer. During irradiation, the solution exhibited an absorbance spectrum for ZnO–TiO_2, visible visually or through the absorbance spectra at 400–600 nm. The degradation time for each sample varied due to the charge particles ability to produce hydroxyl and superoxide radicals, crucial in the photodegradation process. The relationship between the percentage of degradation and irradiation times was established, along with corresponding results for samples prepared with different calcination temperatures and ZnO–TiO_2 concentrations. The absorbance intensity consistently decreased as the time intervals increased, resulting in significant degradation percentages of MB (88.9 %) and RB (84 %) using ZnO–TiO_2. These findings demonstrate the excellent potential of ZnO–TiO_2 composites as photocatalytic materials. The photocatalytic activity was influenced by several factors, including the type of photocatalyst material, crystallite size, and agglomeration level. The photodegradation process is likely influenced by various competing factors. Previous reports have shown that reducing the crystallite size leads to an increase in the specific surface area, which enhances the active reaction of the photocatalyst materials [14].

The ZnO and TiO_2 interface forms a conventional type-II heterojunction, facilitating the migration of photogenerated electrons from the

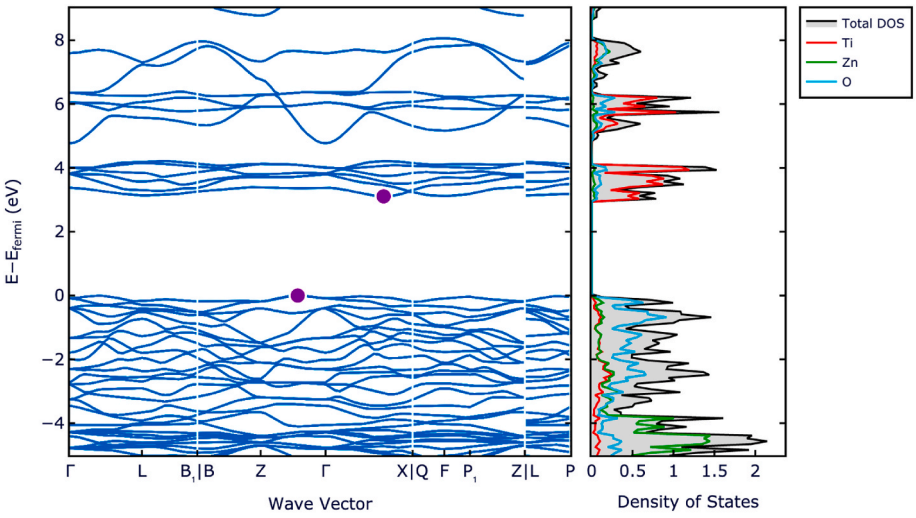

Fig. 10. Band structure and DoS of ZnO–TiO_2.

CB of ZnO to the CB of TiO_2 under UV irradiation. Concurrently, the holes migrate from the VB of TiO_2 to the VB of ZnO, leading to effective spatial separation of the photoinduced electron-hole pairs [53,54]. Despite the fact that the accumulated photogenerated holes in the VB of ZnO are unable to oxidize H_2O to $^{\bullet}OH$ radicals due to the more negative VB edge potential of ZnO compared to the standard redox potential of $^{\bullet}OH/H_2O$ pair, and the accumulated electrons in the CB of TiO_2 cannot reduce O_2 to yield $^{\bullet}O_2^-$ due to the more positive CB of TiO_2 compared to the standard redox potential of $^{\bullet}O_2^-/O_2$ pair, trapping tests have unequivocally demonstrated that $^{\bullet}O_2^-$ and $^{\bullet}OH$ radicals serve as the principal active species in the photocatalytic degradation process, as depicted in Fig. 11 [55].

3.3.1. *Photo-catalytic degradation of MB dye by using synthesized nano catalysts*

Photocatalytic degradation of MB dye with the help of synthesized nanomaterials was verified by UV–Visible spectrometer. The UV–Visible spectroscopy result has shown decrease in the peak of MB at different intervals of time. Initially, the absorption peak of MB was found at λ max 664 nm and at a high absorption value which decreased rapidly on exposure to sunlight, as shown in Fig. 12(a). The completion of the photocatalytic degradation of dye was confirmed when the absorbance

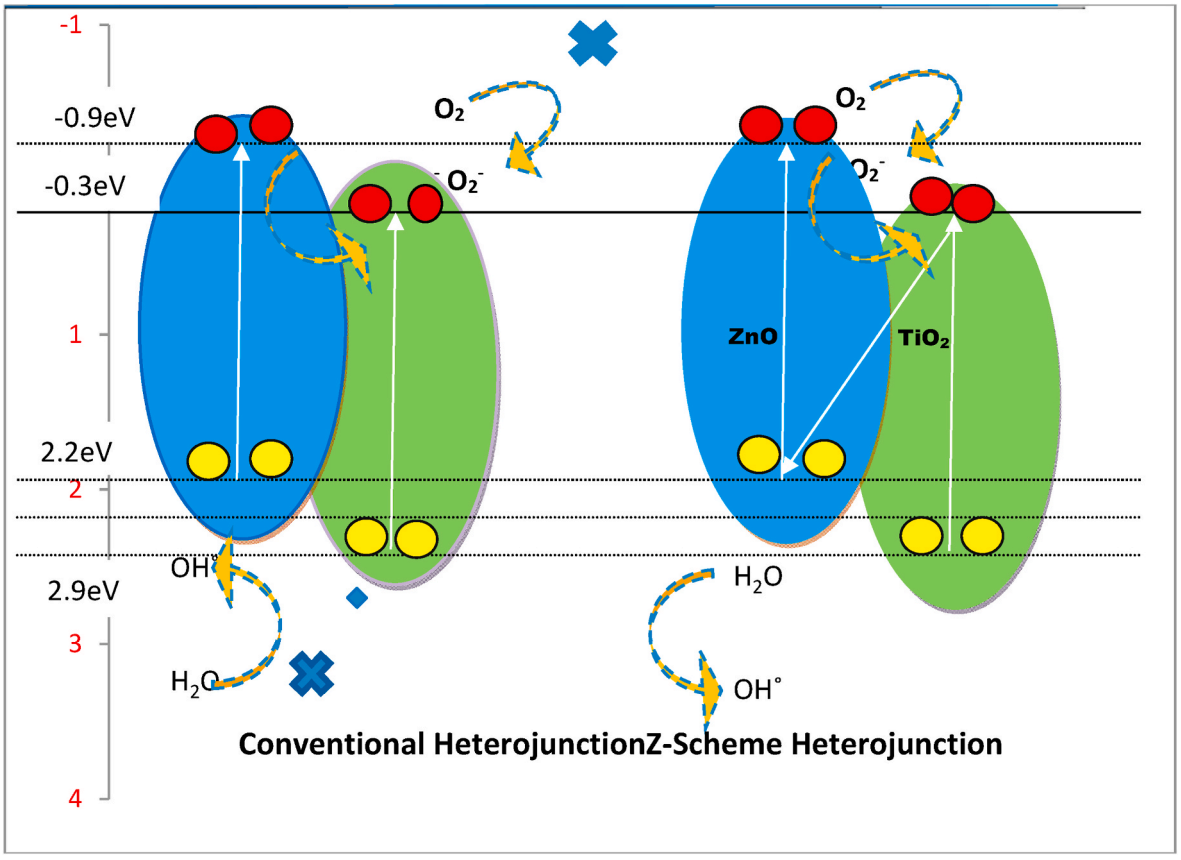

Fig. 11. ZnO–TiO_2 photocatalytic degradation mechanism.

value for the MB peak reaches near the baseline. Amount of degradation of dye in percentage (%) of ZnO was calculated 77 % in 15min, and Fig. 12(b) shows degradation on MB dye with TiO_2 amount of degradation of dye in percentage (%) was found 89.77 % in 15min. while and Fig. 12(c) shows degradation on MB dye with ZnO–TiO_2 amount of degradation of dye in percentage (%) was found 98 % in 15min. and UV–Visible spectroscopy results reveal that dye degrades faster with ZnO–TiO_2 nano-composite than ZnO and TiO_2.

3.3.2. Photo-catalytic degradation of RB dye by using synthesized nano catalysts

Photocatalytic degradation of RB dye with the help of synthesized nanomaterials was verified by UV–Visible spectrometer. The UV–Visible spectroscopy result reveals that the decrease in the peak of RB at different intervals of time, initially, the absorption peak of RB was found at λ max 543 nm and at a high absorption value which decreases rapidly when exposing to sunlight, as shown in Fig. 13(a). The completion of the photocatalytic degradation of dye was conformed when absorbance value for RB peak reach near to baseline. Amount of degradation of dye in percentage (%) of ZnO was calculated 69.66 % in 15 min of exposing time, while with TiO_2 amount of degradation of dye in percentage (%) was found 68.80 % in 15min of exposing time, as shown in Fig. 13(b) while ZnO–TiO_2amount of degradation of dye in percentage (%) was found 79.69 % in 40 min Of solar expose Fig. 13(c) indicates synthesized ZnO–TiO_2have batter photocatalytic activity than ZnO for degrading RB dye.

3.4. Antifungal activity

The assessment of antifungal activity was conducted by measuring the diameter of the zone of inhibition (in mm) for the fungal pathogens *Aspergillus niger* and *Candida albicans*. The results demonstrated varying degrees of antifungal activity for ZnO, TiO_2, and their composite ZnO–TiO_2 NCs, as well as for the positive control, Fluconazole (1 mg/mL).

For *Aspergillus niger*, the diameter of the zone of inhibition for ZnO NPs was approximately 13.0 ± 0.013 mm, while TiO_2 exhibited a slightly smaller zone with a diameter of 12.0 ± 0.012 mm. Notably, the ZnO–TiO_2 composite NPs showed significantly enhanced antifungal activity with a larger zone of inhibition, measuring approximately 28.0 ± 0.12 mm. Fluconazole, a common antifungal agent, displayed a zone of inhibition with a diameter of 26.0 ± 0.034 mm. In the case of *Candida albicans*, ZnO-NPs demonstrated a zone of inhibition with a diameter of 27.0 ± 0.021 mm, while TiO_2 exhibited a slightly smaller zone,

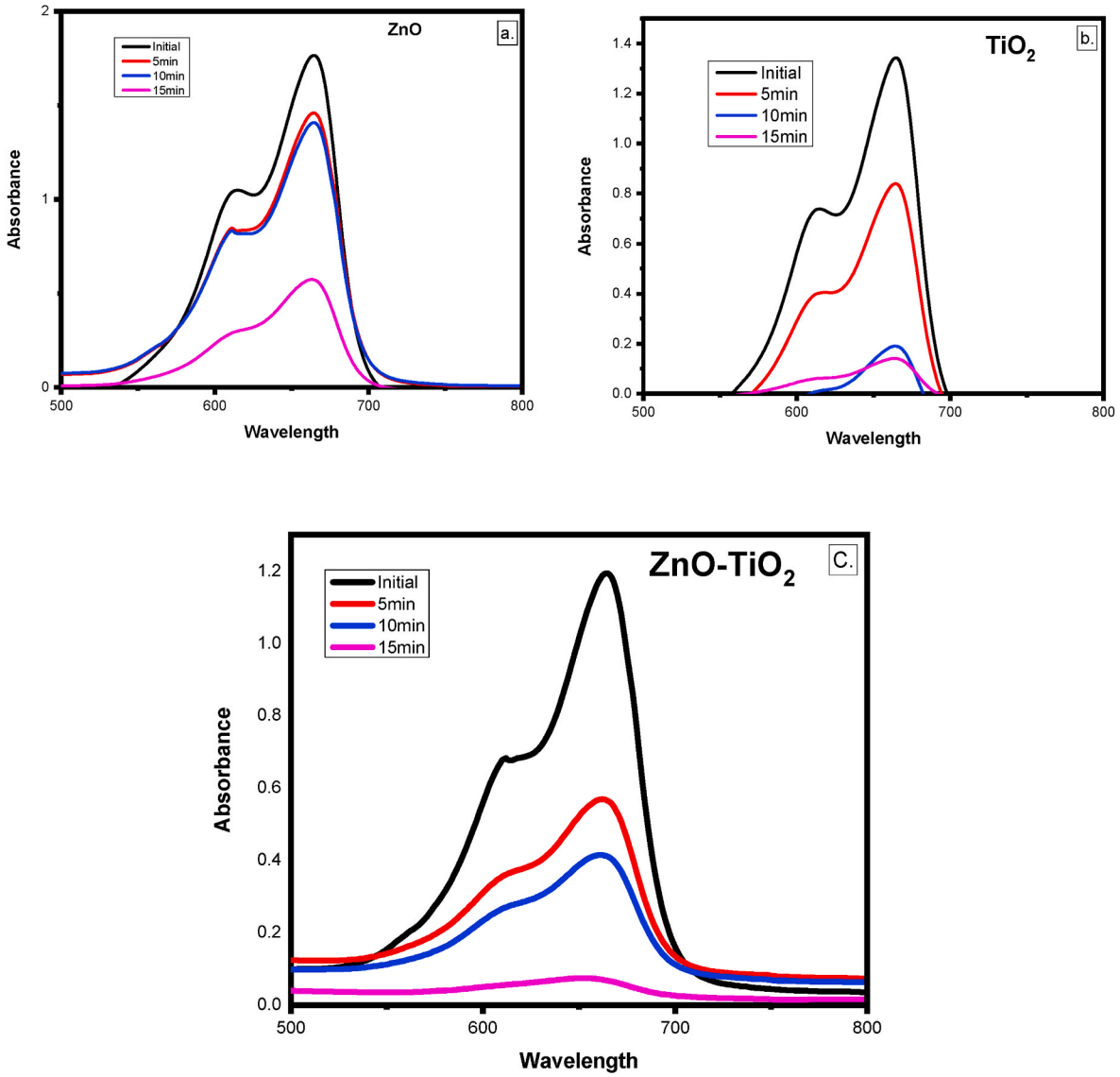

Fig. 12. (a). Degradation of MB in presence of ZnO(b). Degradation of MB in presence of TiO_2 (c). Degradation of MB using ZnO–TiO_2.

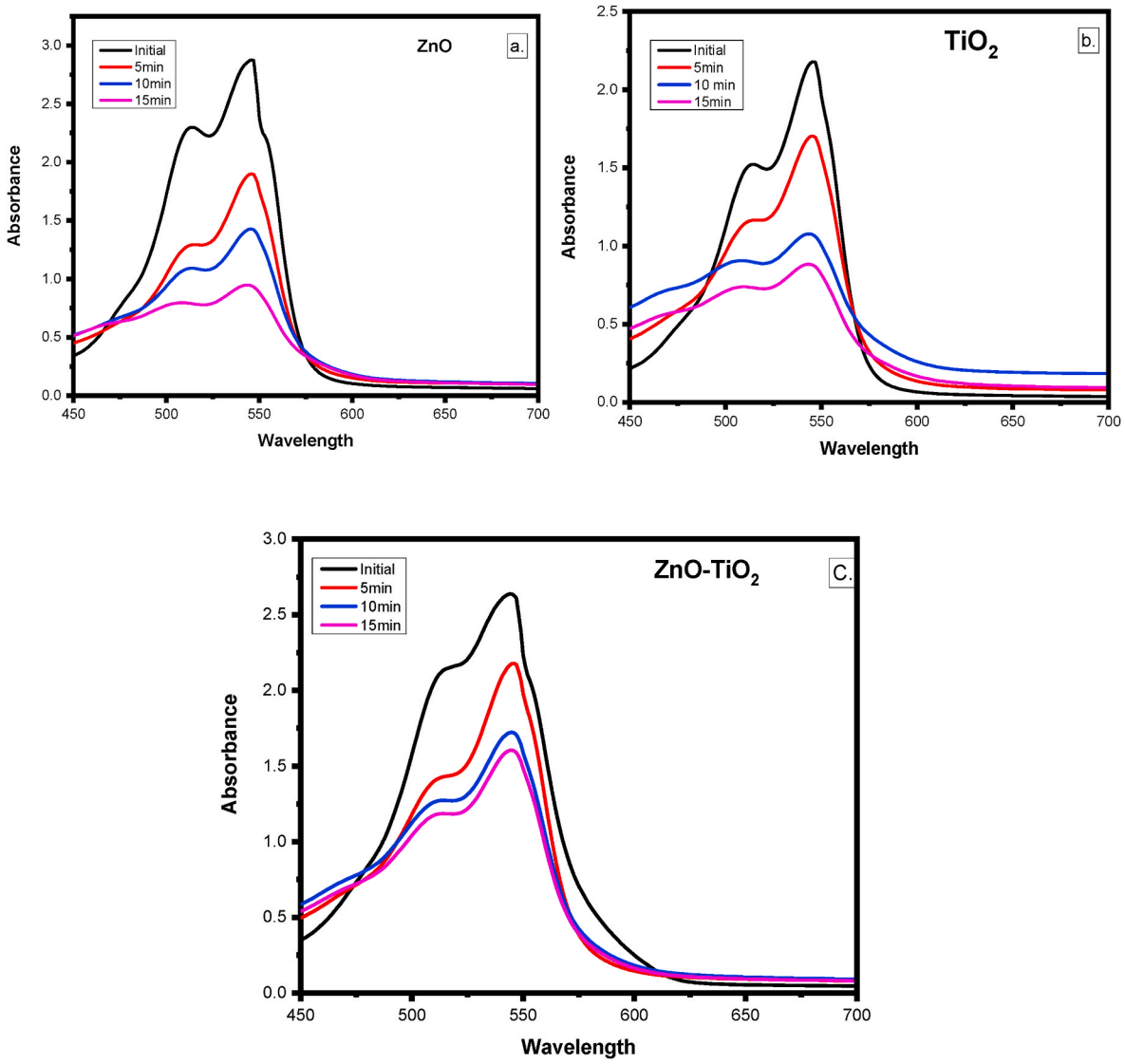

Fig. 13. (a). Degradation of MB in presence of ZnO (b). Degradation of MB in presence of TiO_2(c). Degradation of MB using ZnO–TiO_2.

measuring 25.0 ± 0.027 mm. The ZnO–TiO_2 composite NPs again displayed superior antifungal activity with a zone of inhibition measuring approximately 30.23 ± 0.68 mm. Fluconazole exhibited an inhibition zone diameter of 32.0 ± 0.038 mm.

Conversely, DMSO, used as the negative control, did not exhibit any antifungal activity, resulting in no measurable zone of inhibition. These results indicate that the ZnO–TiO_2 composite NPs possess notably higher antifungal activity compared to individual ZnO and TiO_2NPs for both *Aspergillus niger* and *Candida albicans*. The enhanced antifungal potential observed in the ZnO–TiO_2 composite could be attributed to synergistic effects resulting from the combination of these NPs. These findings emphasize the promising antifungal properties of the ZnO–TiO_2 composite, holding potential for effective antifungal applications in the medical and environmental sectors.

Diameter of Zone of inhibition (mm)		
Test samples/Controls	Test organisms	
	Aspergillus niger	Candida albicans
ZnO	13.0 ± 0.013	27.0 ± 0.021
TiO_2	12.0 ± 0.012	25.0 ± 0.027
ZnO–TiO_2	28.0 ± 0.12	30.23 ± 0.68
Fluconazole (1 mg/mL)	26.0 ± 0.034	32.0 ± 0.038
DMSO	NA	NA

4. Conclusion

In conclusion, our study successfully synthesized a TiO_2–ZnO heterojunction composite, revealing distinct optical and structural properties. The observed red-shift in absorption peaks, along with experimentally determined optical band gaps of 2.3 eV for pure TiO_2 and 2.2 eV for ZnO- nanoparticles (NPs), affirmed the successful composite formation and aligned with established literature. X-ray diffraction analysis showcased robust lattice interactions and the presence of the $ZnTiO_3$ phase, further validating the composite's dual-phase composition, with precise lattice spacing values. Fourier transform infrared spectroscopy shed light on the composite's functional groups, while thermal analysis provided insights into its stability through distinct weight loss regions. Energy-dispersive X-ray and transmission electron microscopy analysis has confirmed uniform element distribution and a regular macroporous structure within TiO_2, adding to the comprehensive characterization.

The computational study utilizing density functional theory enriched our understanding by offering a phase diagram and band structures. Remarkably, the composite displayed exceptional photocatalytic

activity, achieving significant degradation percentages for Methylene Blue and Rose Bengal. Furthermore, the ZnO–TiO_2 composite exhibited superior antifungal activity against *Aspergillus niger* and *Candida albicans*, surpassing individual NPs and even the positive control, Fluconazole. These collective findings underscore the promising attributes of composites in terms of optics, structure, photocatalysis, and antifungal efficacy, paving the way for its potential applications in various scientific and technological domains.

Ethical approval

I confirm that the research presented in the manuscript has obtained ethical approval and complies with all ethical guidelines and regulations.

Consent to participate

I voluntarily agree to take part in the research study. I understand the research purpose and procedures. My participation is entirely of my own choice, and I may withdraw at any time.

Consent to publish

I, Dr. Aayasha Negi on behalf of all my coauthors grant permission to publish data.

CRediT authorship contribution statement

Mohamed Taha Yassin: Funding acquisition, Data curation. **Aayasha Negi:** Conceptualization. **Sumit Ringwal:** Formal analysis. **Minakshi Pandey:** Methodology. **Prabhat Sati:** Visualization, Software. **Prashast Kumar Tripathi:** Investigation.

Declaration of competing interest

The authors declares no conflict of interest.

Data availability

No data was used for the research described in the article.

Acknowledgments

The authors extend their appreciation to the Researchers Supporting Project number (RSPD2024R1105), King Saud University, Riyadh, Saudi Arabia.

References

[1] T.A. Saleh, M. Mustaqeem, M. Khaled, Water treatment technologies in removing heavy metal ions from wastewater: a review, Environ. Nanotechnol. Monit. Manag. 17 (2022) 100617.
[2] A. Hojjati-Najafabadi, et al., Magnetic-MXene-based nanocomposites for water and wastewater treatment: a review, J. Water Proc. Eng. 47 (2022) 102696.
[3] J.O. Eniola, et al., A review on conventional and advanced hybrid technologies for pharmaceutical wastewater treatment, J. Clean. Prod. 356 (2022) 131826.
[4] J. Zhao, et al., Tannery wastewater treatment: conventional and promising processes, an updated 20-year review, J. Leather Sci. Eng. 4 (1) (2022) 10.
[5] A. Singh, et al., Biological remediation technologies for dyes and heavy metals in wastewater treatment: new insight, Bioresour. Technol. 343 (2022) 126154.
[6] A. Negi, P. Rana, D.S. Negi, Multi dye degradation, antibacterial, antidiabetic and antioxidant assessment of silver nanoparticles (Ag-NPs) derived via leaves of Smilax aspera, Inorg. Chem. Commun. 143 (2022) 109703.
[7] H. Alamgholiloo, et al., Facile fabrication of Z-scheme TiO2/ZnO@ MCM-41 heterojunctions nanostructures for photodegradation and bioactivity performance, J. Mol. Liq. 364 (2022) 119990.
[8] B. Chen, et al., Rational design of all-solid-state TiO2-x/Cu/ZnO Z-scheme heterojunction via ALD-assistance for enhanced photocatalytic activity, J. Colloid Interface Sci. 607 (2022) 760–768.
[9] X. Lian, et al., Constructing Z-scheme 1D/2D heterojunction of ZnIn2S4 nanosheets decorated WO3 nanorods to enhance Cr (VI) photocatalytic reduction and rhodamine B degradation, Chemosphere 313 (2023) 137351.
[10] J. Hongxia, et al., A new double Z-scheme TiO2/ZnO-g-C3N4 nanocomposite with enhanced photodegradation efficiency for Rhodamine B under sunlight, Environ. Prog. Sustain. Energy 42 (1) (2023) e13968.
[11] S. Kumar, R. Kaushik, L. Purohit, RGO supported ZnO/SnO2 Z-scheme heterojunctions with enriched ROS production towards enhanced photocatalytic mineralization of phenolic compounds and antibiotics at low temperature, J. Colloid Interface Sci. 632 (2023) 196–215.
[12] Hung, C., et al., Direct Z-Scheme Heterostructure of In-Situ Planted Zno Nanorods on G-C3n4 Thin Sheets Sprayed on Tio2 Layer: A Strategy for Ternary-Photoanode Engineering towards Enhanced Photoelectrochemical Water Splitting. Available at: SSRN 4401316.
[13] L. Wang, C. Bie, J. Yu, Challenges of Z-scheme photocatalytic mechanisms, Trends in Chemistry 4 (11) (2022) 973–983.
[14] J. Abdul Nasir, et al., Photocatalytic Z-scheme overall water splitting: recent advances in theory and experiments, Adv. Mater. 33 (52) (2021) 2105195.
[15] T. Zhou, et al., Bird-nest structured ZnO/TiO2 as a direct Z-scheme photoanode with enhanced light harvesting and carriers kinetics for highly efficient and stable photoelectrochemical water splitting, Appl. Catal. B Environ. 267 (2020) 118599.
[16] T. Wang, et al., Direct utilization of air and water as feedstocks in the photo-driven nitrogen reduction reaction over a ternary Z-scheme SiW 9 Co 3/PDA/BWO heterojunction, J. Mater. Chem. A 8 (32) (2020) 16590–16598.
[17] A. Chawla, et al., An overview of SnO_2 based Z scheme heterojuctions: fabrication, mechanism and advanced photocatalytic applications, J. Ind. Eng. Chem. 116 (2022) 515–542.
[18] C. Liu, et al., Photo-Fenton degradation of tetracycline over Z-scheme Fe-g-C3N4/Bi2WO6 heterojunctions: mechanism insight, degradation pathways and DFT calculation, Appl. Catal. B Environ. 310 (2022) 121326.
[19] M.Q. Qader, Y.A. Shekha, Application of two fungal strains Aspergillus Niger and Candida albicans in wastewater quality improvement, J. Edu. Sci. 31 (4) (2022) 33–41.
[20] B.A. Hemdan, et al., Green sol–gel synthesis of novel nanoporous copper aluminosilicate for the eradication of pathogenic microbes in drinking water and wastewater treatment, Environ. Sci. Pollut. Control Ser. 26 (2019) 9508–9523.
[21] M. Safaei, M. Taran, M.M. Imani, Preparation, structural characterization, thermal properties and antifungal activity of alginate-CuO bionanocomposite, Mater. Sci. Eng. C 101 (2019) 323–329.
[22] M. Ghosh, et al., Enhanced antifungal activity of fluconazole conjugated with Cu-Ag-ZnO nanocomposite, Mater. Sci. Eng. C 106 (2020) 110160.
[23] J. Wang, et al., ZnO nanoparticles implanted in TiO2 macrochannels as an effective direct Z-scheme heterojunction photocatalyst for degradation of RhB, Appl. Surf. Sci. 456 (2018) 666–675.
[24] Y. Zhou, et al., Construction of urchin-like ZnO/TiO2 direct Z-scheme system to improve charge separation, ChemistrySelect 4 (44) (2019) 12963–12970.
[25] N. Jomehzadeh, et al., Investigating in-vitro antimicrobial activity, biosynthesis, and characterization of silver nanoparticles, zinc oxide nanoparticles, and silver-zinc oxide nanocomposites using Pistacia Atlantica Resin, Mater. Today Commun. 27 (2021) 102457.
[26] P. Arabkhani, et al., Plant extracts-mediated green synthesis of zinc oxide/carbon nanofiber nanocomposites with highly efficient photocatalytic and antimicrobial properties for wastewater treatment, J. Water Proc. Eng. 54 (2023) 104020.
[27] A. Negi, et al., Biogenic zinc oxide nanoparticles as an antibacterial, antifungal, and photocatalytic tool mediated via leaves of Girardinia diversifolia, Nanotechnology for Environmental Engineering 7 (1) (2022) 223–233.
[28] A. Negi, R.K. Vishwakarma, D.S. Negi, Synthesis and evaluation of antibacterial, anti-fungal, anti-inflammatory properties of silver nanoparticles mediated via roots of Smilax aspera, Mater. Today: Proc. 57 (2022) 27–33.
[29] S. Dalkılıç, et al., In vitro cytotoxic effects of Smilax aspera L. roots on cancer cell lines, Food Biosci. 46 (2022) 101501.
[30] Selmi, H., et al., Phytochemical screening, antioxidant activity and in vitro fermentation from smilax aspera, rhamnus alaternus and CALYCOTUM villosa from ewes and goats. 'Proceeding Book': p. 304.
[31] M. Abd El-Kader, et al., Morphological, structural and antibacterial behavior of eco-friendly of ZnO/TiO2 nanocomposite synthesized via Hibiscus rosa-sinensis extract, J. Mater. Res. Technol. 15 (2021) 2213–2220.
[32] G. Rizqillah, et al., Band gap energy calculation of theaflavin and cyanidin-3-glucoside molecules as active material in dye sensitized solar cells using density functional theory (DFT), in: Journal of Physics: Conference Series, IOP Publishing, 2021.
[33] B. Illés, et al., Incorporation and corrosion protection mechanism of TiO2 nanoparticles in SnAgCu composite alloys: experimental and density functional theory study, Ceram. Int. 49 (14) (2023) 23765–23774.
[34] S. Ringwal, A.S. Bartwal, S.C. Sati, Photo-catalytic degradation of different toxic dyes using silver nanoparticles as photo-catalyst, mediated via Citrus aurantium peels extract, J. Indian Chem. Soc. 98 (12) (2021) 100221.
[35] T. Bavani, et al., Construction of direct Z-scheme g-C3N4/BiYWO6 heterojunction photocatalyst with enhanced visible light activity towards the degradation of methylene blue, Environ. Sci. Pollut. Control Ser. 30 (4) (2023) 10179–10190.
[36] P. Sasikala, et al., A Z-scheme BiYO3/g-C3N4 heterojunction photocatalyst for the degradation of organic pollutants under visible light irradiation, Environ. Sci. Pollut. Control Ser. 30 (14) (2023) 41095–41106.
[37] T. Bavani, et al., One-pot synthesis of bismuth yttrium tungstate nanosheet decorated 3D-BiOBr nanoflower heterostructure with enhanced visible light photocatalytic activity, Chemosphere 297 (2022) 133993.

[38] T. Bavani, et al., One-step synthesis of rod-on-plate like 1D/2D-NiMoO4/BiOI nanocomposite for an efficient visible light driven photocatalyst for pollutant degradation, Environ. Sci. Pollut. Control Ser. 29 (43) (2022) 65222–65232.
[39] S.S. Hosseini, et al., Antifungal activity of ZnO nanoparticles and nystatin and downregulation of SAP1-3 genes expression in fluconazole-resistant Candida albicans isolates from vulvovaginal candidiasis, Infect. Drug Resist. (2020) 385–394.
[40] C.H. Nguyen, et al., Enhanced removal of various dyes from aqueous solutions by UV and simulated solar photocatalysis over TiO2/ZnO/rGO composites, Separ. Purif. Technol. 232 (2020) 115962.
[41] Q. Jiang, et al., Preparation and photocatalytic properties of ZnO nano-crack tube in TiO2 micro-burst tube by soaking and calcination after electrospinning, Mater. Lett. 287 (2021) 129272.
[42] X. Li, et al., Synthesis and characterization of ZnO and TiO2 hollow spheres with enhanced photoreactivity, Mater. Sci. Eng., B 158 (1–3) (2009) 40–47.
[43] M. Manzoli, A. Chiorino, F. Boccuzzi, Decomposition and combined reforming of methanol to hydrogen: a FTIR and QMS study on Cu and Au catalysts supported on ZnO and TiO2, Appl. Catal. B Environ. 57 (3) (2005) 201–209.
[44] E. Alizadeh, H. Baseri, Photocatalytic degradation of sumatriptan succinate by ZnO, Fe doped ZnO and TiO2-ZnO nanocatalysts, Mate. Chem. Horizons 1 (1) (2022) 7–21.
[45] S. Lohumi, et al., Quantitative analysis of Sudan dye adulteration in paprika powder using FTIR spectroscopy, Food Addit. Contam. 34 (5) (2017) 678–686.
[46] N. Matijaković Mlinarić, et al., Exposure of microplastics to organic matter in waters enhances microplastic encapsulation into calcium carbonate, Environ. Chem. Lett. 20 (4) (2022) 2235–2242.
[47] L.-K. Chu, Y.-H. Huang, Y.-P. Lee, Step-scan FTIR techniques for investigations of spectra and dynamics of transient species in gaseous chemical reactions, in: Molecular and Laser Spectroscopy, Elsevier, 2022, pp. 481–527.
[48] Z. Liu, et al., Research on moisture content detection method during green tea processing based on machine vision and near-infrared spectroscopy technology, Spectrochim. Acta Mol. Biomol. Spectrosc. 271 (2022) 120921.
[49] M. Chen, et al., Removal of Pb (II) and V (V) from aqueous solution by glutaraldehyde crosslinked chitosan and nanocomposites, Chemosphere 297 (2022) 134084.
[50] S. Ramakrishnan, D.L. Singaravelu, V. Senthilkumar, Microstructure and chemical state analysis of Ti-6Al-4V alloy during abrasive water jet machining process, in: Recent Advances in Materials Technologies: Select Proceedings of ICEMT 2021, Springer, 2022, pp. 607–617.
[51] S.B. Pillai, et al., Understanding the water-in-salt to salt-in-water characteristics across the zinc chloride: water phase diagram, J. Phys. Chem. B 126 (11) (2022) 2265–2278.
[52] F.L. Nordstrom, et al., Enantiotropic inconstancy, crystalline solid solutions and co-crystal in the salicylic acid–anthranilic acid system, Phys. Chem. Chem. Phys. 24 (43) (2022) 26485–26498.
[53] Negi, A., et al., Z-scheme Heterojunction Photocatalyst Potential of TiO2 Implanted with ZnO for Wastewater Treatment. Available at: SSRN 4521720.
[54] M. Shah, et al., ZnO/MgZnO heterostructure membrane with type II band alignment for ceramic fuel cells, Energy Mater 2 (2022) 200031.
[55] P. Kumari, et al., Engineering Schottky-like and heterojunction materials for enhanced photocatalysis performance–a review, Materials Advances 3 (5) (2022) 2309–2323.